Research Square

Preprints are preliminary reports that have not undergone peer review.
They should not be considered conclusive, used to inform clinical practice,
or referenced by the media as validated information.

Transmembrane helix 8 as the main allosteric mediator of CFTR gating revealed by molecular dynamics

Odalys Torres
Semmelweis University
Orsolya Gereben
Semmelweis University
Giovanni Marzaro
University of Verona
Gergely L. Lukacs
McGill University
Tamás Hegedűs
hegedus@hegelab.org

Semmelweis University

Research Article

Keywords: CFTR, allosteric pathways, pore opening, selectivity filter, clustering, interdomain communication

Posted Date: March 2nd, 2026

DOI: https://doi.org/10.21203/rs.3.rs-8787223/v1

License: This work is licensed under a Creative Commons Attribution 4.0 International License.
Read Full License

Additional Declarations: No competing interests reported.

Abstract

Background

The cystic fibrosis transmembrane conductance regulator (CFTR) is a chloride channel whose dysfunction underlies cystic fibrosis. Despite major advances in therapies, a detailed mechanistic understanding of CFTR gating remains essential for the rational development of next-generation drugs and for predicting mutation- and drug-specific effects. While recent cryo-EM structures captured ATP-bound, phosphorylated CFTR conformations, these experimental structures do not exhibit a continuous open chloride permeation pathway, limiting their direct use for gating analysis and *in silico* drug testing. Recently, open CFTR conformation was generated using molecular dynamics (MD) simulations at elevated membrane potential and characterized by a pronounced kink in transmembrane helix 8 (TM8) and a high channel open probability.

Results

We assessed the structural and dynamical validity of this open conformation using a combination of AlphaFold predictions, targeted MD, and extensive equilibrium MD simulations in lipid bilayers. Our results demonstrate that the TM8 is intrinsically highly dynamic and that the kink emerges spontaneously during equilibrium simulations. The open conformation has a substantially higher open probability as compared to that of the simulations initiated from the phosphorylated CFTR cryo-EM structure (6msm). Furthermore, in the open state, the catalytically active ATP-binding site 2 is allosterically coupled to TM8, based on analyses of residue motion correlations, suggesting a direct communication pathway between nucleotide binding and pore opening.

Conclusions

These results support the physiological relevance of the MD-generated open CFTR conformation and identify TM8 as a dynamic allosteric mediator linking nucleotide binding to pore opening, with lipid environment tuning the underlying gating mechanism.

Introduction

Cystic fibrosis (CF) is a life-threatening inherited disorder caused by mutations in the CFTR gene encoding the cystic fibrosis transmembrane conductance regulator [1]. CFTR is a cAMP-activated, ATP-gated chloride channel belonging to the ATP-binding cassette (ABC) transporter superfamily (ABCC7), expressed primarily on epithelial surfaces of the airways, pancreas, and intestine [2, 3]. The protein comprises two transmembrane domains (TMDs), two nucleotide-binding domains (NBDs), and a regulatory (R) domain phosphorylated by protein kinase A [4]. Loss or reduction of CFTR channel activity leads to defective chloride and bicarbonate transport, resulting in thick mucus, chronic infections, and progressive lung damage [5] .

The introduction of CFTR modulators has significantly improved outcomes for patients carrying frequent mutations such as G551D and ΔF508 [6, 7]. However, the exact molecular mechanisms by which these compounds restore channel function remain incompletely understood. High-resolution cryo-EM structures have captured CFTR in several inward- and outward-facing conformations, including complexes with clinically relevant modulators [6–10]. These structures, however, represent endpoints, a static corrected structure, and the dynamic processes leading to CFTR malfunction upon mutation, and the molecular mechanisms by which small-molecule modulators restore channel gating remain unclear.

CFTR gating and restoration of the functional conformation involve large-scale conformational rearrangements transmitted between the NBDs and the TMDs via intracellular loops (ICLs) and coupling helices (CHs) [11, 12]. The current mechanistic gating model proposes that NBD dimerization upon ATP binding initiates pore opening, while ATP hydrolysis and NBD dissociation lead to closure [13]. Two key interfaces – ICL2/NBD2 and ICL4/NBD1 – serve as gating hubs mediating this allosteric communication [14]. Asymmetric behavior between the catalytic and non-catalytic NBD sites has been reported, suggesting directional and possibly sequential allosteric coupling within the channel [15].

The extracellular selectivity filter, formed primarily by TM1, TM6, TM8, TM11, and TM12, plays a crucial role in determining gating stability and ion conductance. Recent mutagenesis and simulation studies have highlighted residues G103, R334, F337, T338 (TM6), and Y914 (TM8) as key contributors to chloride coordination and selectivity [12, 16–19]. Notably, the hydroxyl groups of T338 and Y914 can form anion–dipole interactions, while R334 stabilizes the permeating ion through salt-bridge formation [18, 20, 21]. The aromatic ring of F337 contributes through anion–π interactions, and G103 provides additional stabilization within the filter [18, 21]. Moreover, mutation of Y914C in TM8 alters chloride permeability and conductance, indicating its importance in coupling the selectivity filter to gating transitions [19].

Despite the growing number of structural and functional insights, an experimentally determined structure of CFTR in its fully open, conducting conformation is still lacking. This limitation hinders our understanding of how small molecules stabilize or restore channel activity, and it constrains *in silico* evaluation and rational design of improved modulators. In this study, we investigate the dynamics and allosteric communication underlying CFTR gating by combining AlphaFold-based modeling and all-atom MD simulations. We specifically focus on the open conformation generated by Pomès *et al.*, obtained under high membrane potential [22], and compare it to the 6msm cryo-EM structure [23] representing a low open-probability state. To support the physiological relevance of this open conformation, we also assessed its dynamics and gating behavior in a pure POPC bilayer rather than in a mixed lipid environment, as proper CFTR gating has been shown to depend on membrane cholesterol. Because the Pomès structure features a pronounced kink in TM8, we further applied 3D bioinformatics approaches, including AlphaFold modeling and MD simulations, to examine the structure and stability of this helical segment.

Results

The unusual kink in TM8. Experimental CFTR structures from the Jue Chen laboratory reveal a distinct kink in TM8, resulting in a unique transmembrane helical arrangement not observed in other ABC protein structures (Fig. 1A) [10, 24, 25]. AlphaFold predictions incorporating structural templates reproduce this kinked conformation with high accuracy (https://alphafold.ebi.ac.uk/entry/P13569). However, when AlphaFold3 is run locally without templates, TM8 appears as a straight helix with high pLDDT scores and is displaced from the rest of the TM bundle, leading to a likely non-physiological conformation (Fig. 1B).

To better understand the kinked TM8 conformation, we performed targeted MD simulations using GROMACS patched with PLUMED [26–28]. Gentle steering forces were applied to minimize the RMSD between the Cα atoms of the simulated protein and those of the 6msm structure. Under these conditions, TM8 remained intact and did not intercalate between neighboring helices (Fig. 1C).

To further test the stability and dynamics of this conformation, where TM8 is already in contact with surrounding helices, we ran unbiased equilibrium MD simulations. Interestingly, in one out of two simulations, TM8 spontaneously unwound and adopted a kinked conformation, intercalating between other helices like the experimental structure (Fig. 1D).

The gating of the open CFTR structure generated by Pomès et al. Since our targeted simulations involved motions opposite to those expected during channel gating - namely, starting from a non-physiological AlphaFold conformation and forcing TM8 inward - we did not consider the resulting conformations suitable as starting points for studying gating. Instead, we regarded the approach of Pomès *et al.* [29], who applied − 500 mV membrane potential to induce a physiologically realistic open conformation. From their simulations conducted at a low membrane potential (− 17 mV), we selected a representative open-channel structure (frame 651, f651). This conformation and the 6msm cryo-EM structure were embedded in a mixed lipid bilayer, energy-minimized, and used to initiate two independent 2-μs simulations for each construct in the absence of membrane potential. To identify opening events and chloride permeation pathways, the resulting trajectories were analyzed using HOLE2.

Based on our previous experience, the high mobility of the extracellular and intracellular regions tends to obscure the observations of closure events in the transmembrane (TM) region. To address this, we restricted the HOLE2 analysis to the pore segment between residues 192, 985, and 1155 located at the intracellular leaflet of the membrane bilayer, and residues 104, 335, and 1131 in the extracellular half (Fig. 2A). Pathways with a minimum pore radius ≥ 1.8 Å were classified as open to chloride ions, and the open probability (P□) was calculated as the ratio of frames with open pathways to all analyzed frames (2 × 200,000). Simulations initiated from the 6msm structure (Fig. 2B) displayed low open probability (P□ = 0.00033). In contrast, conformations from f651 trajectories showed markedly higher fractions of open states (Fig. 2C), yielding P□ = 0.233 and 0.657.

To further assess the physiological relevance of the open conformations generated by Pomès *et al.*, we performed additional simulations in bilayers composed solely of POPC. As CFTR gating has been shown to depend on cholesterol [30, 31], we expected lower P_o values compared to those obtained in mixed lipid environments. Indeed, reduced open probabilities (0.227 and 0.166) were observed in the POPC-

only simulations (Fig. 3A). The difference between P_o values obtained in POPC and mixed bilayers was evaluated using bootstrapping (ΔP(6msm–f651) = − 0.443, 95% CI = [− 0.657, − 0.232], n = 10,000).

Next, we examined the effect of modeled extracellular loops on gating, as they could potentially bias the system toward open or closed states. The calculated P_o = 0.005 for simulations based on 6msm with modeled loops (Fig. 3B) was slightly higher than that obtained from the original 6msm runs (P_o = 0.00033, Fig. 2B), but the difference was not statistically significant (ΔP(6msm–6msm-loops) = − 0.004, 95% CI = [− 0.009, 0.000], *n* = 10,000).

Finally, we identified the bottleneck residues defining the narrowest regions of the chloride permeation pathway in all open conformations across the simulated systems. Residues located within 4.5 Å of the smallest HOLE2 spheres were considered part of the constriction region. In simulations initiated from the 6msm structure, which exhibited low open probabilities, the bottleneck residues (a.a. 102, 106, 109, 337, 1134) located in the TM1 and TM6 helices were found in most frames with open conformations (≥ 30%) and were positioned more extracellularly (Fig. 4A) than in the f561 conformation derived from simulations by Pomès *et al.* [22] (Fig. 4B). In trajectories starting from this open conformation, residues 102, 341, and 1137 consistently formed part of the constriction region in most frames. Interestingly, in f561 systems embedded in bilayers composed exclusively of POPC lipids, the narrowest segments were observed at the extracellular ends of the helices (a.a. 109, 334, and 1126; Fig. 4C). An intracellular shift of the constriction region was detected in the 6msm simulations supplemented with modeled loop regions (Fig. 4D), where the narrowest section comprised residues 99, 102, 103, 106, 337, 338, and 341, somewhat similar location of observed for f561 (Fig. 4B).

Allosteric communication in ATP-bound inward-closed CFTR conformations. To explore allosteric coupling across different CFTR systems, equilibrium MD trajectories were segmented and analyzed using a mutual information–based approach to quantify residue–residue motion correlations [32]. Based on these correlations, the shortest communication pathways were computed between residue Q1291 positioning the γ-phosphate of ATP and the pore-lining residue Y914, thereby mapping potential routes connecting the catalytic ATP-binding site to the TMD gating region, defined here as the extracellular pore bottleneck formed by Y914 and its surrounding pore-lining residues.

In simulations initiated from the low open probability 6msm conformation, the most frequently traversed allosteric pathways between the two residues involved NBD2 residues (1251, 1255, 1260, 1283, and 1370), coupling helix 2 (272 and 276), and TM6 (333) (Fig. 5A). Most of these residues appeared in at least half of the identified pathways, except for 1370, which is spatially close to the source residue 1290 and was present in all cases. In contrast, pathways observed in the f651 open-channel simulations included NBD2 residues (1251, 1255, 1260, 1291, and 1371), residues in the intracellular region of TM8 (946, 950, 954, 958), a hydrophobic stretch in TM9 (988, 992, 996, 1000), and residues in the extracellular part of TM8 (915, 919, 923, 927) (Fig. 5B). Notably, the shift toward TM9 bypasses the kink-forming residues in TM8.

When the same f651 conformation was simulated in a POPC-only bilayer (Fig. 5C), high-frequency pathway residues (> 0.5) were mainly found in TM5 (282, 290, 294, 298, 302, 305, 306, 310, and 314), whereas residues in TM8 and TM9 remained involved but with lower frequencies, consistent with weakened long-range coupling in the absence of membrane cholesterol. Finally, the presence of modeled loop regions in 6msm had no appreciable impact on allosteric pathway propagation, as similar routes were observed in the loop-deleted model (Fig. 5D).

Discussion

CFTR gating is a highly dynamic, multiscale process that links ATP binding and hydrolysis at the nucleotide-binding domains to conformational rearrangements in the transmembrane helices forming the chloride permeation pathway [2, 11, 19, 20, 24, 33]. While experimental structures have been indispensable for defining CFTR architecture, their limited representation of fully open states [12, 13, 18, 22, 31, 34] necessitates complementary *in silico* approaches to capture functionally relevant gating conformations [12, 13, 22, 31, 35, 36].

We first evaluated the structural basis of the open CFTR conformation proposed by Pomès *et al.* [22, 34], focusing on the pronounced kink in TM8. AlphaFold predictions indicated intrinsic flexibility in TM8 (Fig. 1A), suggesting that this region is predisposed to conformational rearrangement. Importantly, equilibrium MD simulations initiated from remodeled structures demonstrated that the TM8 kink can develop spontaneously, supporting the notion that this feature is not an artifact of sample preparation for cryo-EM [37] but rather a dynamically accessible state of the protein.

Consistent with this structural rearrangement, simulations of the open structure generated in high electric field [22, 34, 38] exhibited a markedly higher channel P_o than simulations initiated from the ATP-bound 6msm structure [13, 22, 29, 34]. Analysis of chloride permeation pathways (Figs. 2 to 4) revealed a wider and more persistent conductive pathway over the course of the simulations, indicating stabilization of the open conformation of the putative outer pore and selectivity filter, in agreement with functional expectations for an open channel [18, 24, 39, 40].

To link these structural changes to CFTR's regulatory machinery, we analyzed residue motion correlations and allosteric communication pathways. In the open conformations, the catalytically active ATP-binding site 2 showed strong allosteric connectivity to TM8 and neighboring transmembrane segments (Fig. 5). This coupling to the gating region was substantially weaker in the low-open-probability simulations, indicating that TM8 plays a critical role in transmitting nucleotide-binding signals to the pore region.

To further assess the physiological relevance of these observations, we examined the impact of membrane composition by performing simulations in pure POPC bilayers. Consistent with experimental data showing that CFTR gating is modulated by cholesterol [30], POPC-only simulations displayed reduced open probabilities and weakened long-range allosteric coupling compared to simulations in mixed lipid bilayers (Figs. 3A and 5C). Importantly, however, both pore opening and allosteric

communication pathways responded coherently to the altered lipid environment, TM8-centered communication routes remained detectable, albeit with reduced frequency, indicating that the observed coupling itself is not specific to a particular membrane composition. Rather, membrane composition appears to tune the strength of this allosteric coupling.

Beyond open probability, the axial position of the pore constriction differed systematically across the simulated systems and provided additional mechanistic insight into CFTR gating (Fig. 4). In simulations initiated from the low-open-probability 6msm structure, the narrowest region of the chloride pathway was predominantly located toward the extracellular side of the pore, consistent with a labile, partially conductive state in which closure occurs near the selectivity filter. In contrast, simulations of the f651 open conformation in mixed lipid bilayers exhibited a constriction shifted toward the center of the membrane (Fig. 4), indicative of a more stabilized open channel architecture. This centralization of the constriction region was partially reversed in POPC-only bilayers, where the narrowest segment again localized closer to the extracellular side. This shift mirrors the reduced open probability and weakened long-range allosteric coupling observed in the absence of cholesterol, suggesting that membrane composition influences not only how often the channel opens, but also where along the pore axis closure is most likely to occur. Together, these results indicate that the spatial position of the constriction region constitutes a sensitive structural marker of gating stability and allosteric reinforcement.

We also assessed the contribution of extracellular loop regions to gating and allosteric signaling by comparing simulations with and without modeled loops. The presence of extracellular loops did not substantially alter channel open probability (Fig. 3B), nor did it redirect or focus allosteric communication pathways toward TM8 (Fig. 5D), however, exhibited an inward shift of the constriction region toward the bilayer center, partially resembling the behavior of the f651 open conformation (Fig. 4D). These findings suggest that extracellular loops can bias the spatial positioning of the gating barrier within the pore, potentially by modulating local pore geometry or extracellular vestibule dynamics but are insufficient on their own to stabilize a fully open, highly conductive state. We note, however, that extracellular loops are challenging to model accurately due to their intrinsic flexibility and limited experimental constraints. Moreover, other unresolved regulatory regions, including the intracellular R domain and the C-terminal tail, were not included in our simulations and may act cooperatively with extracellular loops to fine-tune gating. In the absence of these additional elements, models constructed with or without extracellular loops are therefore expected to sample broadly similar conformational landscapes in MD simulations and to yield comparable outcomes in gating and allosteric pathway analyses.

In conclusion, our results support a model in which TM8 acts as a dynamic allosteric mediator of CFTR gating, with its kinked conformation representing a physiologically relevant open state. The strong coupling between ATP-binding site 2 and TM8 may provide a mechanistic framework for understanding how nucleotide binding, mutations, and small-molecule modulators influence channel opening. These findings underscore the value of integrative computational approaches for dissecting CFTR gating and offer a validated structural platform for future *in silico* studies aimed at rational drug design.

Methods

AlphaFold predictions. CFTR structural model was downloaded from the AlphaFold Structure Database (https://alphafold.ebi.ac.uk/entry/AF-P13569-F1) [41, 42]. AlphaFold3 was also installed locally to make predictions without using structural templates.

System preparation for MD simulations. Initial structures for MD simulations with CFTR were the phosphorylated 6msm structure [23] and open conformation generated by Pomès *et al.* A conformation (frame 651, f651) from the trajectory generated at the lowest membrane potential (-17 mV) [22]. A CFTR structure with modelled extracellular loops was also generated [43, 44]. All protein structures were oriented using the PPM server (Orientation of Proteins in Membranes, OPM) [45] and were capped with acetyl (ACE) groups at the N-termini and N-methylamide (CT3) groups at the C-termini. For lipid bilayer embedding, two membrane compositions were prepared, including a mixed bilayer to represent a physiological cell membrane and a pure POPC bilayer. The extracellular leaflet of the mixed bilayer consisted of cholesterol, POPC (1-palmitoyl-2-oleoyl-sn-glycerol-3-phosphocholine), PLPC (1-palmitoyl-2-linoleoyl-sn-glycerol-3-phosphocholine), and SSM (Sphingomyelin) in a 25:30:30:15 ratio, while the intracellular leaflet comprised cholesterol, POPC, PLPC, POPE (1-palmitoyl-2-oleoyl-sn-glycerol-3-phosphoethanolamine), POPS (1-palmitoyl-2-oleoyl-sn-glycerol-3-phospho-L-serine), and PIP2 (DMPI25, dimyristoyl-phosphatidylinositol 2,5) in a 24:24:24:14:8:5 ratio. The system was neutralized with 150 mM KCl and solvated with TIP3P water. Four systems were generated in total: (1) 6msm in a mixed bilayer, (2) 6msm in a POPC bilayer, (3) 6msm with modelled extracellular loops in a mixed bilayer, and (4) f561 in a mixed bilayer.

Equilibrium MD simulations. System input files for energy minimization, equilibration, and production runs were generated using the CHARMM-GUI web interface [46]. All simulations employed the CHARMM36m all-atom force field [47]. Energy minimization was performed using the steepest descent integrator, with a maximum of 50,000 steps or until convergence was achieved with a force threshold below 1,000 kJ/mol/nm. The Berendsen thermostat and barostat were used for the equilibration steps, while the v-rescale thermostat and C-rescale barostat were applied during production runs. Pressure coupling was semi-isotropic, maintained at 1 ATM with a time constant of 5 ps in the membrane plane and a compressibility of 4.5×10^{-5} bar^{-1}. Long-range interactions were truncated at 12 Å, and electrostatic interactions were computed using the smooth Particle Mesh Ewald (PME) method [48]. Bond constraints were applied via the LINCS algorithm with a maximum bond length of 1.2 nm [49]. All simulations were performed in the NPT ensemble (constant particle number, pressure, and temperature) using a 2-fs time step in GROMACS 2022.5 [47, 50, 51]. Two 2 μs long runs for each system were initiated with random velocities.

Channel pore analysis. Trajectory frames for all systems were aligned based on Cα atoms to the initial structure. Every frame was extracted as a pdb file for analysis with HOLE2 to evaluate pore geometry [52]. From the resulting profiles, the transmembrane region defined by intracellularly (192, 985, and 1155)

and extracellularly (104, 335, and 1131) located residues was examined. Channels possessing a minimum radius of 1.8 Å (3.6 Å diameter) throughout the simulation were identified.

Targeted MD simulation. To drive the AlphaFold-predicted inward-open CFTR structure toward an inward-closed (6msm-like) conformation, we performed targeted MD simulations using GROMACS 2021 patched with PLUMED 2.8 [26–28]. The AF3-predicted structure was embedded in a mixed lipid bilayer, energy-minimized, and equilibrated as described above. Targeted MD was then applied by restraining the RMSD between the Cα atoms of the simulated structure and the 6msm reference structure using the MOVINGRESTRAINT bias. The target RMSD was progressively reduced from 5.86 Å to 0 Å over 80 ns, while the KAPPA (the force constant of the harmonic biasing potential applied to the RMSD collective variable, defining the strength with which the system is steered toward the target reference structure) was gradually increased based on continuous monitoring of the simulation stability. Using a maximum KAPPA value of 22,000, the RMSD could be reduced to approximately 2 Å without introducing major structural distortions.

Allosteric pathway determination. To characterize allosteric communication within CFTR, equilibrium MD trajectories were analysed using a network-based approach derived from residue motion correlations [53]. For each system, two independent production trajectories were considered. From each trajectory, the time window between 1 and 2 μs was extracted and subdivided into overlapping segments of 200 ns duration, yielding a total of 18 segments per system. This segmentation strategy was chosen to improve statistical robustness while preserving sensitivity to dynamical heterogeneity across the trajectories.

For each segment, trajectories were aligned to a common reference frame using Cα atoms to remove global translation and rotation. Residue-residue motion correlations were then calculated independently for each segment using the generalized correlation formalism based on mutual information, as introduced by Lange and Grubmüller [54]. This measure captures both linear and nonlinear correlations in atomic motions and was computed using the implementation provided in the wordom package [55]. Allosteric networks were constructed by representing amino acid residues as nodes and pairwise motion correlations as weighted edges. Edge weights were defined as $-\log(C_{ij})$, where C_{ij} denotes the generalized correlation coefficient between residues i and j, such that strongly correlated residue pairs correspond to shorter effective distances in the network. For each segment, shortest communication pathways were calculated between predefined source and target residues using the networkx Python library [56]. Residues participating in the shortest paths were extracted using in-house Python scripts, and their frequencies of occurrence across all segments were calculated. Pathway statistics were aggregated over all segments and both trajectories to generate frequency-weighted representations of allosteric communication for each simulated system.

Analysis. Coordinates from trajectories, pore profiles from HOLE2 output were extracted using in-house Python scripts. All molecular figures were generated using PyMOL [57].

Abbreviations

ABC
ATP-Binding Cassette
ACE
Acetyl groups
CF
Cystic Fibrosis
CFTR
Cystic Fibrosis Transmembrane Regulator
CH
Coupling Helices
CHL1
Cholesterol
CT3
N-methylamide
DMPI25
dimyristoyl-phosphatidylinositol 2,5
ICL
Intracellular Loops
MD
Molecular Dynamics
NBD
Nucleotide Binding Domain
NPT
Isothermal–isobaric ensemble
OPM
Orientation of Proteins in Membranes
PME
Particle Mesh Ewald
pLDDT
predicted Local Distance Difference Test
PLPC
1-palmitoyl-2-linoleoyl-sn-glycerol-3-phosphocholine
POPC
1-palmitoyl-2-oleoyl-sn-glycerol-3-phosphocholine
POPE
1-palmitoyl-2-oleoyl-sn-glycerol-3-phosphoethanolamine
POPS
1-palmitoyl-2-oleoyl-sn-glycerol-3-phospho-L-serine
PPM
Positioning of proteins in membranes

SSM
Sphingomyelin
TM
Transmembrane
TMD
Transmembrane Domain

Declarations

There was no conflict of interest within this research.

Ethics approval and consent to participate - not applicable, NA

Consent for publication - not applicable, NA

Availability of data and materials

The datasets generated and/or analyzed during the current study are available in the Zenodo repository: https://doi.org/10.5281/zenodo.18430675

Funding

This work was supported by the Italian Cystic Fibrosis Foundation (grant FFC#1/2024 to G.M., G.L.L. and T.H.) and the National Research, Development and Innovation Office, Hungary [K 137610, TKP2021-EGA-23, and HU-RIZONT-2024-00003].

Authors' contributions

KT: Writing – original draft, Investigation, Methodology

OG: Writing – review and editing, Investigation

GM: Writing – review and editing,

GL: Conceptualization, Writing – review and editing,

TH: Conceptualization, Investigation, Methodology, Funding acquisition, Writing – original draft

Acknowledgements

We acknowledge the computational resources made available on the Komondor GPU cluster of the Governmental Information-Technology Development Agency and on GPU cluster of Wigner Scientific Computation Laboratory, HUN-REN Wigner RCP.

References

1. Bombieri C, Seia M, Castellani C. Genotypes and Phenotypes in Cystic Fibrosis and Cystic Fibrosis Transmembrane Regulator–Related Disorders. Semin Respir Crit Care Med. 2015;36:180–93. https://doi.org/10.1055/s-0035-1547318.
2. Schultz BD, Singh AK, Devor DC, Bridges RJ. Pharmacology of CFTR Chloride Channel Activity. Physiological Reviews. 1999;79:S109–44. https://doi.org/10.1152/physrev.1999.79.1.S109.
3. Saint-Criq V, Gray MA. Role of CFTR in epithelial physiology. Cell Mol Life Sci. 2017;74:93–115. https://doi.org/10.1007/s00018-016-2391-y.
4. Devidas S, Guggino WB. CFTR: Domains, Structure, and Function. J Bioenerg Biomembr. 1997;29:443–51. https://doi.org/10.1023/A:1022430906284.
5. Pilewski JM, Frizzell RA. Role of CFTR in Airway Disease. Physiological Reviews. 1999;79:S215–55. https://doi.org/10.1152/physrev.1999.79.1.S215.
6. Lopes-Pacheco M. CFTR Modulators: The Changing Face of Cystic Fibrosis in the Era of Precision Medicine. Front Pharmacol. 2019;10:1662. https://doi.org/10.3389/fphar.2019.01662.
7. Harutyunyan M, Huang Y, Mun K-S, Yang F, Arora K, Naren AP. Personalized medicine in CF: from modulator development to therapy for cystic fibrosis patients with rare CFTR mutations. American Journal of Physiology-Lung Cellular and Molecular Physiology. 2018;314:L529–43. https://doi.org/10.1152/ajplung.00465.2017.
8. Hwang T-C, Yeh J-T, Zhang J, Yu Y-C, Yeh H-I, Destefano S. Structural mechanisms of CFTR function and dysfunction. J Gen Physiol. 2018;150:539–70. https://doi.org/10.1085/jgp.201711946.
9. Callebaut I, Chong PA, Forman-Kay JD. CFTR structure. Journal of Cystic Fibrosis. 2018;17:S5–8. https://doi.org/10.1016/j.jcf.2017.08.008.
10. Fiedorczuk K, Chen J. Molecular structures reveal synergistic rescue of Δ508 CFTR by Trikafta modulators. Science. 2022;378:284–90. https://doi.org/10.1126/science.ade2216.
11. Infield DT, Strickland KM, Gaggar A, McCarty NA. The molecular evolution of function in the CFTR chloride channel. J Gen Physiol. 2021;153:e202012625. https://doi.org/10.1085/jgp.202012625.
12. Mornon J-P, Lehn P, Callebaut I. Molecular models of the open and closed states of the whole human CFTR protein. Cell Mol Life Sci. 2009;66:3469–86. https://doi.org/10.1007/s00018-009-0133-0.
13. Vergani P, Lockless SW, Nairn AC, Gadsby DC. CFTR channel opening by ATP-driven tight dimerization of its nucleotide-binding domains. Nature. 2005;433:876–80. https://doi.org/10.1038/nature03313.
14. Chong PA, Kota P, Dokholyan NV, Forman-Kay JD. Dynamics intrinsic to cystic fibrosis transmembrane conductance regulator function and stability. Cold Spring Harb Perspect Med. 2013;3:a009522. https://doi.org/10.1101/cshperspect.a009522.
15. Ayca E, Bengi A, Nurit LL, Nir B-T, Turkan H, Oded L. Computational analysis of long-range allosteric communications in CFTR. 2023. https://doi.org/10.7554/eLife.88659.2.

16. Farinha CM, Callebaut I. Molecular mechanisms of cystic fibrosis - how mutations lead to misfunction and guide therapy. Biosci Rep. 2022;42:BSR20212006. https://doi.org/10.1042/BSR20212006.
17. Callebaut I, Hoffmann B, Lehn P, Mornon J-P. Molecular modelling and molecular dynamics of CFTR. Cell Mol Life Sci. 2017;74:3–22. https://doi.org/10.1007/s00018-016-2385-9.
18. Levring J, Chen J. Structural identification of a selectivity filter in CFTR. Proc Natl Acad Sci USA. 2024;121:e2316673121. https://doi.org/10.1073/pnas.2316673121.
19. Negoda A, Hogan MS, Cowley EA, Linsdell P. Contribution of the eighth transmembrane segment to the function of the CFTR chloride channel pore. Cell Mol Life Sci. 2019;76:2411–23. https://doi.org/10.1007/s00018-019-03043-2.
20. Linsdell P. Mechanism of chloride permeation in the cystic fibrosis transmembrane conductance regulator chloride channel. Experimental Physiology. 2006;91:123–9. https://doi.org/10.1113/expphysiol.2005.031757.
21. Sippel KH, Quiocho FA. Ion-dipole interactions and their functions in proteins. Protein Sci. 2015;24:1040–6. https://doi.org/10.1002/pro.2685.
22. Zeng Z-W, Ing CE, Pomès R. Structure and Cl- Conductance Properties of the Open State of Human CFTR. 2025. https://doi.org/10.7554/eLife.105722.
23. Zhang Z, Liu F, Chen J. Phosphorylated, ATP-bound human cystic fibrosis transmembrane conductance regulator (CFTR): 6msm. 2018. https://doi.org/10.2210/pdb6msm/pdb.
24. Farkas B, Tordai H, Padányi R, Tordai A, Gera J, Paragi G, et al. Discovering the chloride pathway in the CFTR channel. Cell Mol Life Sci. 2020;77:765–78. https://doi.org/10.1007/s00018-019-03211-4.
25. Levring J, Terry DS, Kilic Z, Fitzgerald G, Blanchard SC, Chen J. CFTR function, pathology and pharmacology at single-molecule resolution. Nature. 2023;616:606–14. https://doi.org/10.1038/s41586-023-05854-7.
26. Bonomi M, Branduardi D, Bussi G, Camilloni C, Provasi D, Raiteri P, et al. PLUMED: A portable plugin for free-energy calculations with molecular dynamics. Computer Physics Communications. 2009;180:1961–72. https://doi.org/10.1016/j.cpc.2009.05.011.
27. Tribello GA, Bonomi M, Branduardi D, Camilloni C, Bussi G. PLUMED 2: New feathers for an old bird. Computer Physics Communications. 2014;185:604–13. https://doi.org/10.1016/j.cpc.2013.09.018.
28. The PLUMED consortium. Promoting transparency and reproducibility in enhanced molecular simulations. Nat Methods. 2019;16:670–3. https://doi.org/10.1038/s41592-019-0506-8.
29. Zeng ZW, Linsdell P, Pomès R. Molecular dynamics study of Cl- permeation through cystic fibrosis transmembrane conductance regulator (CFTR). Cell Mol Life Sci. 2023;80:51. https://doi.org/10.1007/s00018-022-04621-7.
30. Chin S, Ramjeesingh M, Hung M, Ereño-Oreba J, Cui H, Laselva O, et al. Cholesterol Interaction Directly Enhances Intrinsic Activity of the Cystic Fibrosis Transmembrane Conductance Regulator (CFTR). Cells. 2019;8:804. https://doi.org/10.3390/cells8080804.

31. Aleksandrov LA, Jensen TJ, Cui L, Kousouros JN, He L, Aleksandrov AA, et al. Thermal stability of purified and reconstituted CFTR in a locked open channel conformation. Protein Expression and Purification. 2015;116:159–66. https://doi.org/10.1016/j.pep.2015.09.018.
32. Diez G, Nagel D, Stock G. Correlation-Based Feature Selection to Identify Functional Dynamics in Proteins. J Chem Theory Comput. 2022;18:5079–88. https://doi.org/10.1021/acs.jctc.2c00337.
33. Broadbent SD, Ramjeesingh M, Bear CE, Argent BE, Linsdell P, Gray MA. The cystic fibrosis transmembrane conductance regulator is an extracellular chloride sensor. Pflugers Arch - Eur J Physiol. 2015;467:1783–94. https://doi.org/10.1007/s00424-014-1618-8.
34. Zeng ZW, Pomès R. Structure and dynamics of chloride ion conduction in CFTR. Biophysical Journal. 2024;123:401a. https://doi.org/10.1016/j.bpj.2023.11.2457.
35. Callebaut I, Hoffmann B, Lehn P, Mornon J-P. Molecular modelling and molecular dynamics of CFTR. Cell Mol Life Sci. 2017;74:3–22. https://doi.org/10.1007/s00018-016-2385-9.
36. Wang J, Jain A, McDonald LR, Gambogi C, Lee AL, Dokholyan NV. Mapping allosteric communications within individual proteins. Nat Commun. 2020;11:3862. https://doi.org/10.1038/s41467-020-17618-2.
37. Tordai H, Leveles I, Hegedűs T. Molecular dynamics of the cryo-EM CFTR structure. Biochemical and Biophysical Research Communications. 2017;491:986–93. https://doi.org/10.1016/j.bbrc.2017.07.165.
38. Zeng ZW, Linsdell P, Pomès R. Molecular dynamics study of Cl− permeation through cystic fibrosis transmembrane conductance regulator (CFTR). Cell Mol Life Sci. 2023;80:51. https://doi.org/10.1007/s00018-022-04621-7.
39. Linsdell P. Architecture and functional properties of the CFTR channel pore. Cell Mol Life Sci. 2017;74:67–83. https://doi.org/10.1007/s00018-016-2389-5.
40. El Hiani Y, Negoda A, Linsdell P. Cytoplasmic pathway followed by chloride ions to enter the CFTR channel pore. Cell Mol Life Sci. 2016;73:1917–25. https://doi.org/10.1007/s00018-015-2113-x.
41. Fleming J, Magana P, Nair S, Tsenkov M, Bertoni D, Pidruchna I, et al. AlphaFold Protein Structure Database and 3D-Beacons: New Data and Capabilities. Journal of Molecular Biology. 2025;437:168967. https://doi.org/10.1016/j.jmb.2025.168967.
42. Jumper J, Evans R, Pritzel A, Green T, Figurnov M, Ronneberger O, et al. Highly accurate protein structure prediction with AlphaFold. Nature. 2021;596:583–9. https://doi.org/10.1038/s41586-021-03819-2.
43. Fiser A, Šali A. Modeller: Generation and Refinement of Homology-Based Protein Structure Models. In: Methods in Enzymology. Elsevier; 2003. p. 461–91. https://doi.org/10.1016/S0076-6879(03)74020-8.
44. Soya N, Xu H, Roldan A, Yang Z, Ye H, Jiang F, et al. Folding correctors can restore CFTR posttranslational folding landscape by allosteric domain–domain coupling. Nat Commun. 2023;14:6868. https://doi.org/10.1038/s41467-023-42586-8.

45. Lomize MA, Pogozheva ID, Joo H, Mosberg HI, Lomize AL. OPM database and PPM web server: resources for positioning of proteins in membranes. Nucleic Acids Research. 2012;40:D370–6. https://doi.org/10.1093/nar/gkr703.
46. Jo S, Kim T, Iyer VG, Im W. CHARMM-GUI: A web-based graphical user interface for CHARMM. J Comput Chem. 2008;29:1859–65. https://doi.org/10.1002/jcc.20945.
47. Huang J, Rauscher S, Nawrocki G, Ran T, Feig M, de Groot BL, et al. CHARMM36m: an improved force field for folded and intrinsically disordered proteins. Nat Methods. 2017;14:71–3. https://doi.org/10.1038/nmeth.4067.
48. Darden T, York D, Pedersen L. Particle mesh Ewald: An $N \cdot \log(N)$ method for Ewald sums in large systems. The Journal of Chemical Physics. 1993;98:10089–92. https://doi.org/10.1063/1.464397.
49. Hess B, Bekker H, Berendsen HJC, Fraaije JGEM. LINCS: A linear constraint solver for molecular simulations. J Comput Chem. 1997;18:1463–72. https://doi.org/10.1002/(SICI)1096-987X(199709)18:12%253C1463::AID-JCC4%253E3.0.CO;2-H.
50. Abraham MJ, Murtola T, Schulz R, Páll S, Smith JC, Hess B, et al. GROMACS: High performance molecular simulations through multi-level parallelism from laptops to supercomputers. SoftwareX. 2015;1–2:19–25. https://doi.org/10.1016/j.softx.2015.06.001.
51. Brooks BR, Brooks CL, Mackerell AD, Nilsson L, Petrella RJ, Roux B, et al. CHARMM: the biomolecular simulation program. J Comput Chem. 2009;30:1545–614. https://doi.org/10.1002/jcc.21287.
52. Smart OS, Neduvelil JG, Wang X, Wallace BA, Sansom MSP. HOLE: A program for the analysis of the pore dimensions of ion channel structural models. Journal of Molecular Graphics. 1996;14:354–60. https://doi.org/10.1016/S0263-7855(97)00009-X.
53. Hegedus T, Gyimesi G, Gaspar ME, Szalay KZ, Gangal R, Csermely P. Potential Application of Network Descriptions for Understanding Conformational Changes and Protonation States of ABC Transporters. CPD. 2013;19:4155–72. https://doi.org/10.2174/1381612811319230002.
54. Lange OF, Grubmüller H. Generalized correlation for biomolecular dynamics. Proteins. 2006;62:1053–61. https://doi.org/10.1002/prot.20784.
55. Seeber M, Felline A, Raimondi F, Muff S, Friedman R, Rao F, et al. Wordom: a user-friendly program for the analysis of molecular structures, trajectories, and free energy surfaces. J Comput Chem. 2011;32:1183–94. https://doi.org/10.1002/jcc.21688.
56. Hagberg A, Swart P, S Chult D. Exploring network structure, dynamics, and function using NetworkX. Los Alamos National Lab.(LANL), Los Alamos, NM (United States); 2008.
57. Schrödinger L, DeLano W. PyMOL. 2020.

Figures

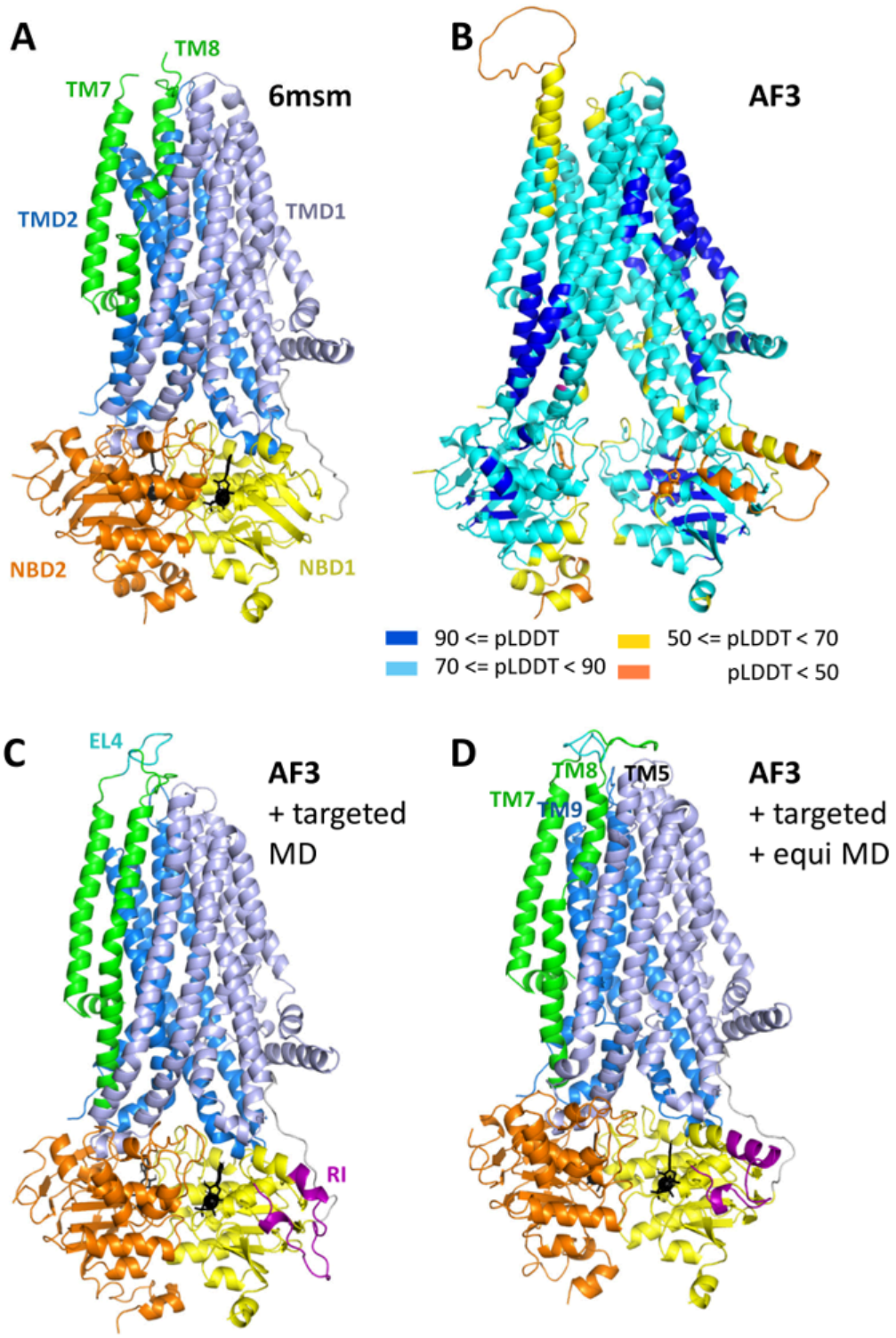


Figure 1

Kink in the TM8 developed in an MD simulation. (A) The cryo-EM structure 6msm was determined under activating conditions. Yellow, orange, light blue, blue, and green indicate NBD1, NBD2, TMD1, TMD2, and TM7/8, respectively. **(B)** AlphaFold3 without structural templates predicts a straight TM8. The structure is colored according to pLDDT scores. **(C)** Targeted MD simulation resulted in closed NBDs (orange and

yellow). TM8 got closer to the other TM helices but remained straight. **(D)** The output of the targeted MD was subjected to equilibrium simulations, exhibiting unwinding of TM8 (green).

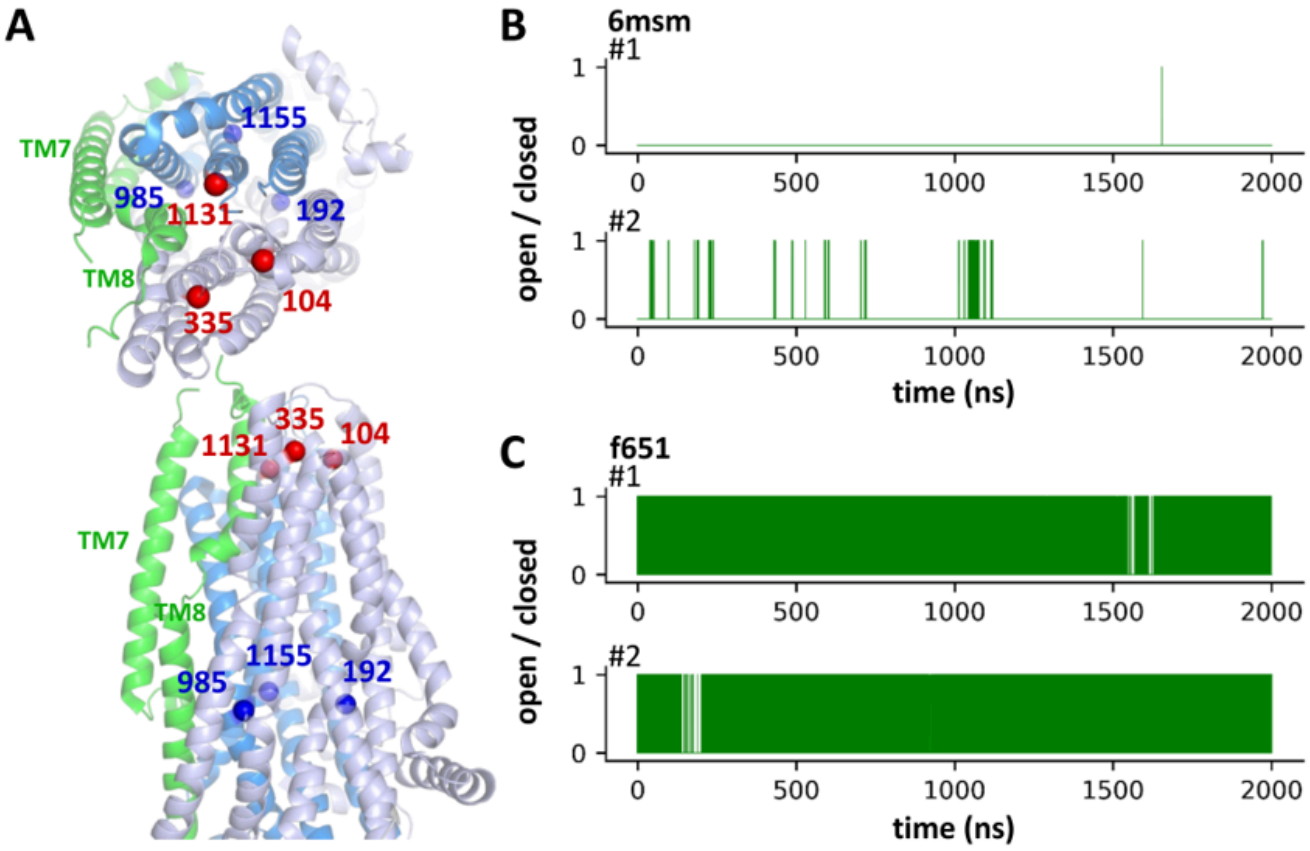


Figure 2

The f651 conformation gates more often than the 6msm structure. (A) The channel diameter was assessed by HOLE between extracellular (a.a. 104, 335, and 1131) and intracellular (a.a. 192, 1155, and 985) residues in all frames. Views from the extracellular space (top) and from the membrane (bottom). Binary (open/closed) single channel like traces of two equilibrium simulations with the 6msm **(B)** and f561 structures**(C)**.

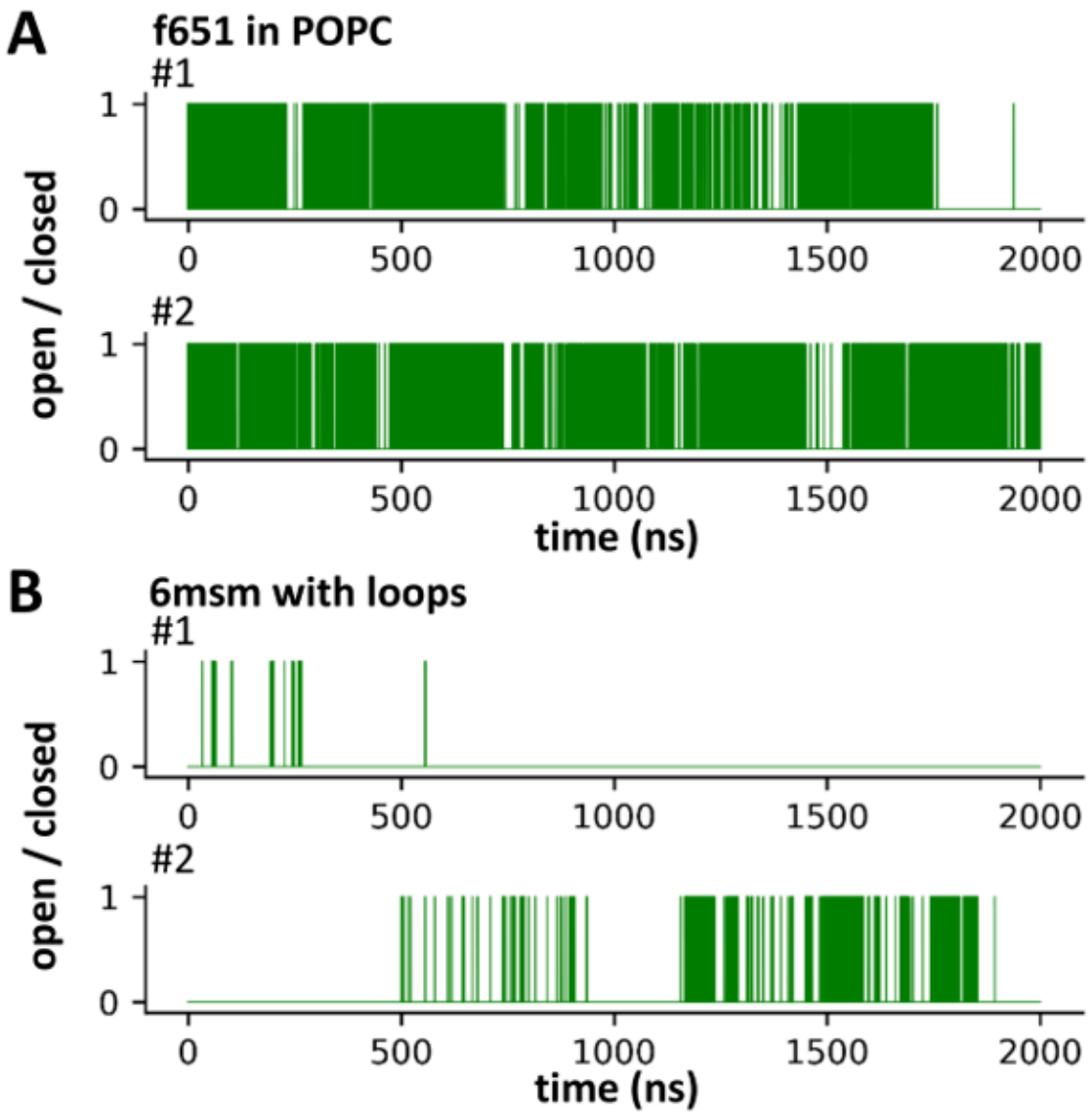


Figure 3

Membrane bilayer lipid composition affects gating. (A) The P_o was significantly decreased in a bilayer containing only POPC when compared to simulations performed in the presence of a bilayer with a complex composition. **(B)** The presence of modelled extracellular loops did not significantly alter the gating.

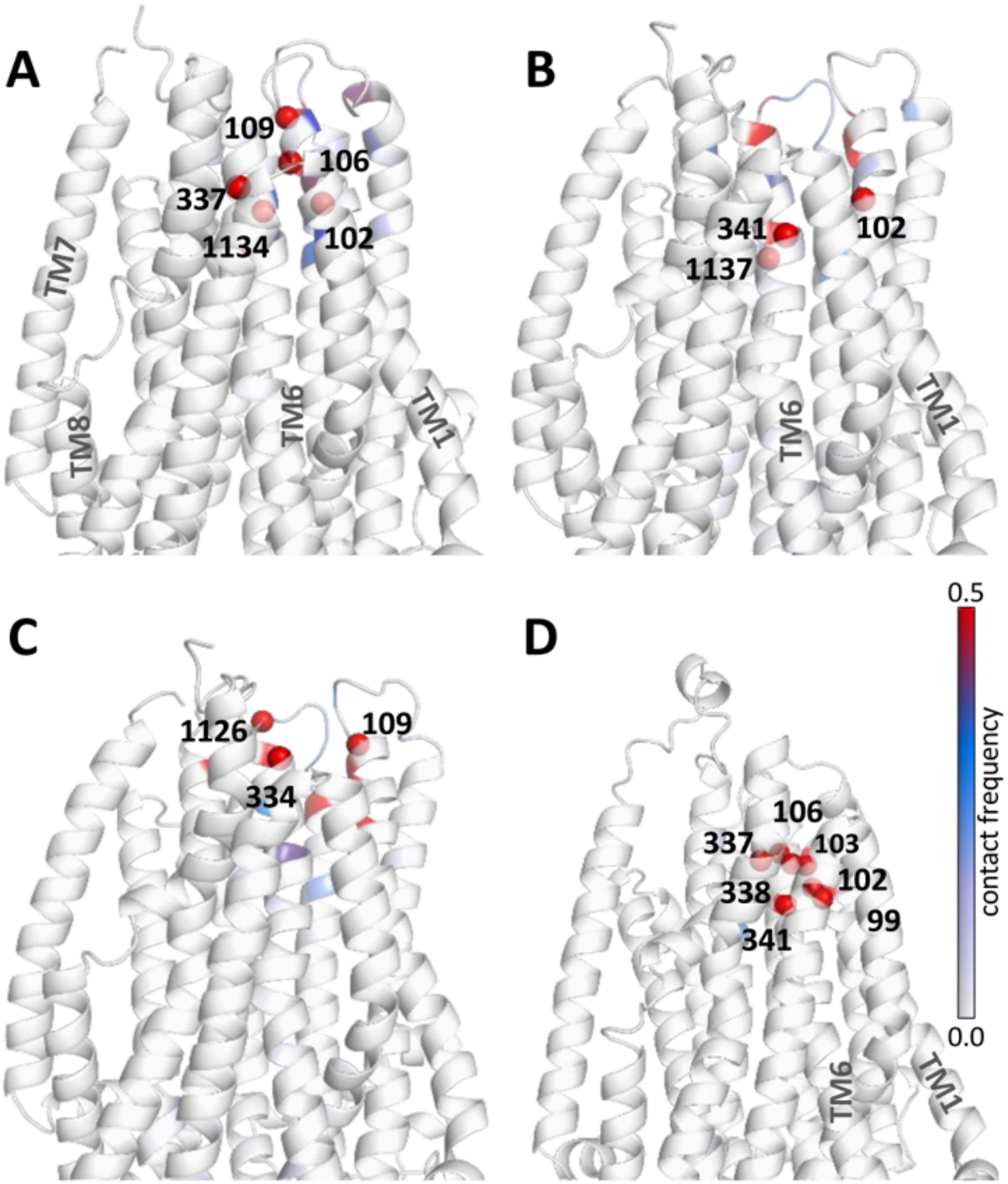


Figure 4

Bottleneck region is located towards the bilayer center in gating systems and in the presence of extracellular loops. The narrowest region along the chloride pathway in 6msm (A), f651 in mixed bilayer (B), f651 in pure POPC lipids (C), and 6msm with modelled extracellular loops (D). Residues closest to the bottleneck regions were counted in all frames and their frequency is color coded. The serial number of the residues with higher occurrence in the narrowest regions are indicated.

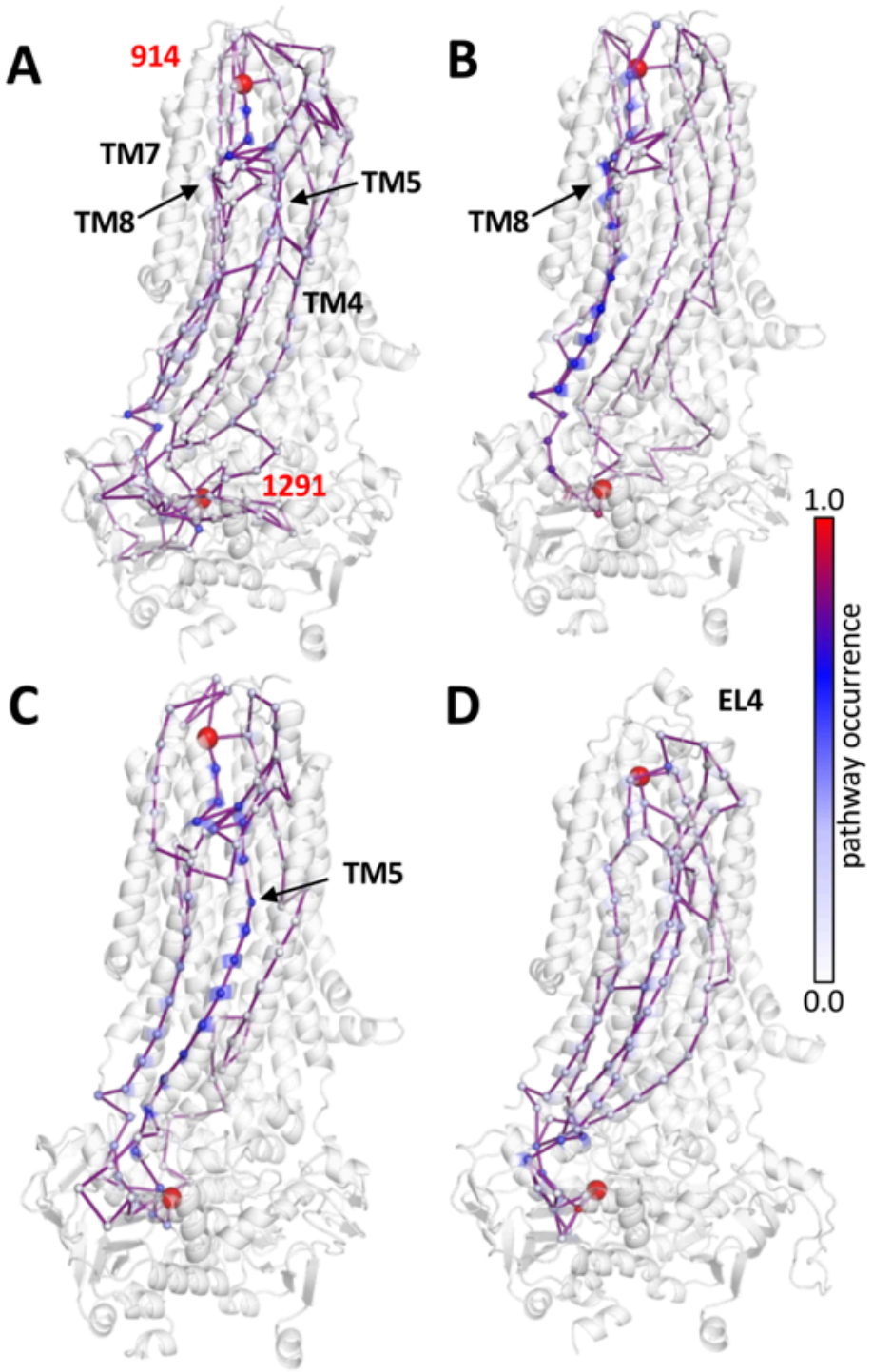


Figure 5

Allosteric communication pathways between catalytic ATP-binding site and the TMD gating region. Allosteric pathways (lines in raspberry between spheres of Cα) between Q1291 and Y914 (larger red spheres) were determined from MD simulations with 6msm (A), f651 (B), f651 in POPC (C), and 6msm with loops (D). Occurrences of residues in pathways were calculated and their frequences were color coded (white, light blue, blue, red from low to higher values).